TECHNICAL ARTICLE

Experimental electron density distribution of KZnB$_3$O$_6$ constructed by maximum-entropy method

Qi Li [1,2,†], Yi Huang,[3,†] Yanfang Lou,[1,†] Munan Hao,[1,2] and Shifeng Jin[1,4,a)]

[1]*The Beijing National Laboratory for Condensed Matter Physics, Institute of Physics, Chinese Academy of Sciences, Beijing 100190, China*

[2]*College of Materials Science and Opto-Electronic Technology, University of Chinese Academy of Sciences, Beijing 101408, China*

[3]*State Key Laboratory of Silicon Materials, Department of Material Science and Engineering, ZheJiang University, Yuhangtang Road No.866, Xihu District, Hangzhou 310058, China*

[4]*School of Physical Sciences, University of Chinese Academy of Sciences, Beijing 101408, China*

The dynamic charge density of KZnB$_3$O$_6$, which contains edge-sharing BO$_4$ units, has been characterized using laboratory and synchrotron X-ray diffraction techniques. The experimental electron density distribution (EDD) was constructed using the maximum-entropy method (MEM) from single crystal diffraction data obtained at 81 and 298 K. Additionally, MEM-based pattern fitting (MPF) method was employed to refine the synchrotron powder diffraction data obtained at 100 K. Both the room-temperature single crystal diffraction data and the cryogenic synchrotron powder diffraction data reveal an intriguing phenomenon: the edge-shared B$_2$O$_2$ ring exhibits a significant charge density accumulation between the O atoms. Further analysis of high-quality single crystal diffraction data collected at 81 K, with both high resolution and large signal-to-noise ratio, reveals no direct O–O bonding within the B$_2$O$_2$ ring. The experimental EDD of KZnB$_3$O$_6$ obtained aligns with the results obtained from *ab-initio* calculations. Our work underscores the importance of obtaining high-quality experimental data to accurately determine EDDs.

I. INTRODUCTION

In the past decades, borate crystals have garnered significant attention due to their diverse applications in nonlinear optical materials, fluorescent materials, and laser crystals (Xu et al., 1995; Wang and Chen, 2010). Boron, with its sp^2 and sp^3 hybridized chemical bonds, can form either BO$_3$ triangles (Wu et al., 2006) or BO$_4$ tetrahedra by binding to oxygen atoms (He et al., 2005). The polymerization of these BO$_3$ and BO$_4$ units gives rise to a wide range of anion groups, resulting in the formation of over 1000 borate compounds with remarkable structural flexibility (Yang et al., 2012). Initially proposed by Ross and Edwards (1967), the prevailing understanding in borate chemistry was that BO$_3$ and BO$_4$ groups could only exist in isolation or be linked by common corners, as dictated by Pauling's 3rd and 4th rules (Pauling, 1929). However, Huppertz's group firstly demonstrated that edge-sharing of BO$_4$ polyhedra can be stabilized under extremely high pressure (8–11 GPa) (Huppertz and von der Eltz, 2002). The later discovery of KZnB$_3$O$_6$ suggested that edge-sharing BO$_4$ polyhedra can even be thermodynamically stable under ambient pressure (Jin et al., 2010; Wu et al., 2010). At high temperatures, KZnB$_3$O$_6$ exhibits an unusual unidirectional thermal expansion, which plays a role in preserving edge-sharing BO$_4$ from disassociation (Lou et al., 2015a, 2015b). In the last decade, numerous new borates have been discovered, with an increasing number of them featuring the unusual presence of edge-sharing [BO$_4$] tetrahedra (Mutailipu et al., 2020). Besides, recent research has demonstrated the limited application of the Pauling's rules (George et al., 2020), thus it is not surprising to find more edge-sharing [BO$_4$] tetrahedra. However, while theoretical calculations have been extensively employed to study these edge-sharing BO$_4$ regions (Yang et al., 2012), the experimental investigation on its chemical bonding and charge density distribution remains scarce.

In KZnB$_3$O$_6$, boron binds to oxygen atoms in the form of a BO$_3$ triangle and a BO$_4$ tetrahedron (Jin et al., 2010). Polymerization of these B–O blocks leads to the formation of anion groups B$_6$O$_{12}$, which consist of two BO$_4$ tetrahedra and four BO$_3$ triangles. The BO$_4$ tetrahedra are edge-shared with each other and further corner-shared by BO$_3$ triangles at their outer vertices. It is worth noting that the O–O distance in the edge-sharing zone is exceptionally short, i.e., less than 2.15 Å. For comparison, Figure 1 shows the distribution of O–O atom distances in 1060 borate compounds collected
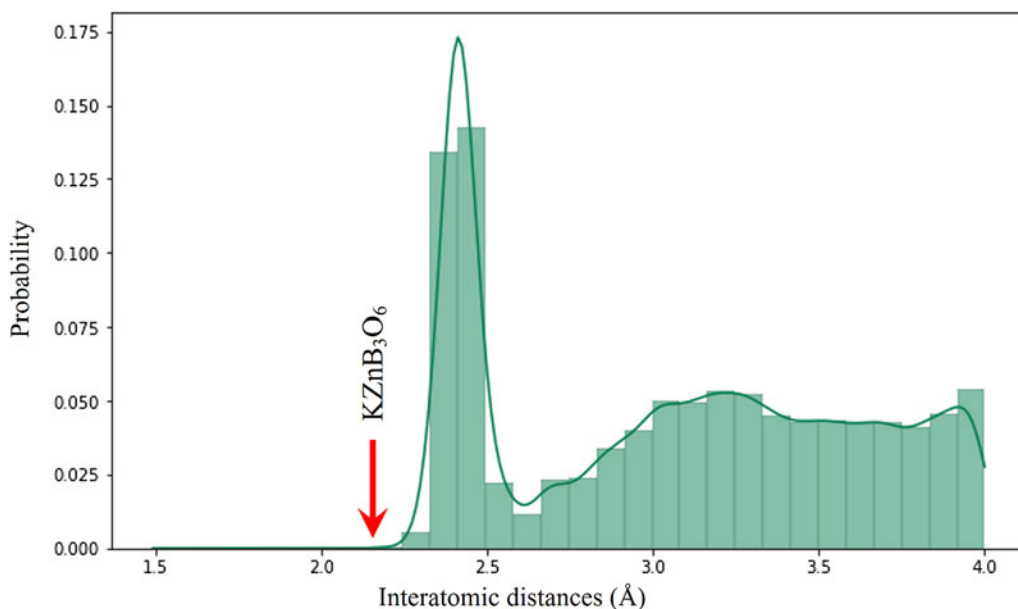

Figure 1. The distribution of O–O atom distances in 1060 borate compounds in the Material Project Database.

from the Material Project Database (Jain et al., 2013), which are predominantly much longer than 2.25 Å. The short O–O distance raises the question of whether there is weak chemical bonding within this edge-sharing region.

Currently, two widely used methods for obtaining experimental charge density from X-ray diffraction data are the multipole refinement method (MM) and the maximum-entropy method (MEM). The MM utilizes multipolar expansions of atomic electron density and offers high-resolution static electron density information (Netzel, 2008). However, the predefined refinable parameters in MM may introduce model-dependent features. In contrast, the MEM reconstructs the electron density distribution (EDD) by maximizing the entropy of the system (Takata et al., 2001). Therefore, MEM does not rely on specific models or functional forms for EDD. This flexibility is particularly valuable when studying materials that exhibit nontraditional bonding, as is the case with the edge-sharing BO_4 unit.

In this study, we utilized synchrotron powder X-ray diffraction (PXRD) to determine the charge density distribution of $KZnB_3O_6$. The crystal structure was refined against the PXRD data using the Rietveld method (Rietveld, 1967). Subsequently, the MEM-based pattern fitting (MPF) method was employed to construct the experimental electron density (Izumi, 2004). It is known that the MEM has the potential to lose structural information due to the overlap of reflections in powder diffraction. Therefore, both room-temperature single crystal X-ray diffraction (SXRD) data (298 K) and high-quality cryogenic SXRD data (81 K) were utilized to construct the charge density using the MEM method. By incorporating these multiple datasets, we aim to capture a comprehensive and accurate representation of the charge density distribution in $KZnB_3O_6$.

II. EXPERIMENTAL METHODS

The single crystal and powder samples of $KZnB_3O_6$ were prepared for diffraction experiments. For SXRD, a Bruker D8 Venture Photo II diffractometer was used to collect the data at

298 K, and a Rigaku XtaLAB Synergy diffractometer was used to collect the data at 81 K. The single crystal structure solution was performed using Olex2 (Dolomanov et al., 2009) and SHELXL (Sheldrick, 2008). The dynamic electron density construction was performed using Dysnomia (Momma et al., 2013). Visualization of crystal structures and charge density maps was achieved using VESTA (Momma and Izumi, 2008). To validate the experimental EDD obtained from the two datasets, we conducted *ab-initio* calculations employing the generalized gradient approximation (GGA) method in the DMol3 package (Delley, 2000).

The PXRD data were collected using the high-resolution powder diffractometer at BL15XU. Synchrotron X-rays from an undulator were monochromatized with a liquid nitrogen-cooled Si (311) double-crystal monochromator, and higher harmonics were reduced using a total reflection mirror system. X-rays with an energy of 29.1947 keV (Sn K edge) were employed. The Debye–Scherrer geometry was utilized, with powder samples loaded into capillaries with a diameter of 0.1 mm. The sample-to-detector distance was 955 mm, ensuring a high angular resolution of 0.003° in 2-theta. Rietveld refinement and the MPF method were conducted using the computer programs RIETAN-FP (Izumi and Momma, 2007) and Dysnomia (Momma et al., 2013).

III. RESULTS AND DISCUSSION

A. Crystal structure refinements

The crystal structure and EDD of $KZnB_3O_6$ were obtained based on two SXRD data sets collected at 298 and 81 K, respectively. The latter dataset collected at a lower temperature is of higher quality, exhibiting a high d-spacing resolution ($d_{min} = 0.50$) and a much higher signal-to-noise ratio ($I/\sigma(I) = 78$) compared to the 298 K data with $d_{min} = 0.65$, $I/\sigma(I) = 27.1$. The crystal structure of $KZnB_3O_6$ was refined using the full-matrix method based on F^2, utilizing the SHELXTL package, and all atoms were refined anisotropically. The refinement process yielded reliability(R) indices of $R_1 =$

2.35%, $wR_2 = 6.35\%$, $R_{int} = 2.04\%$ for the 298 K data, corresponding to completeness of 97.9%, redundancy of 1.22, number of unique reflections of 2112. For the 81 K data, the reliability indices can be further lowered to $R_1 = 1.23\%$, $wR_2 = 3.25\%$, $R_{int} = 1.06\%$, with completeness of 100%, redundancy of 4.20, and number of unique reflections of 4414. The X-ray absorption of both was handled using multi-scan method. More details of SXRD data can be seen in the CIF files deposited as supporting information. Subsequently, the MEM calculations were performed using the Dysnomia package, employing the Limited-memory Broyden–Fletcher–Goldfarb–Shannon (L-BFGS) algorithm to reconstruct the EDD with a grid size of $68 \times 70 \times 70$ pixels in the unit cell.

The structure from PXRD data was further refined in the 2θ range from 3.0 to 30.0° using the Rietveld method implemented in RIETAN-FP. A composite background function based on Legendre polynomials with twelve adjustable parameters was fitted to the background intensities. The pseudo-Voigt function was employed to fit the peak profiles. Attempting to refine the atoms anisotropically led to unstable results for some B atoms and O atoms. Consequently, isotropic atomic displacement parameters were assigned to all atoms. The refinement resulted in reliability (R) indices of $R_p = 3.457\%$, $R_{wp} = 5.235\%$, $S = 6.0700$, $R_B = 6.666\%$, $R_F = 3.163\%$. The results of the Rietveld refinement on the powder diffraction pattern are displayed in Figure 2(d). Finally, the MPF method was applied to obtain the three-dimensional

EDD, with a grid size of $68 \times 70 \times 70$ pixels in the unit cell. After two REMEDY cycles, the reliability indices decreased to $R_B = 2.847\%$ and $R_F = 1.493\%$, respectively.

The crystal structure of $KZnB_3O_6$, depicted in Figure 2, reveals a unit cell consisting of 22 atoms. The compound maintains its inversion symmetry (space group P-1) between temperatures of 81 K and 298 K. As illustrated in the inset of Figure 2(d), this compound exhibits two edge-sharing BO_4 units, comprising two corner-shared B_3O_3 rings connected by a B_2O_2 ring. The refined cell parameters obtained through various methods are summarized in Table I. The unit cell volume increases from 269.646 to 272.68 $Å^3$ between 81 and 298 K. The structural parameters for single crystal $KZnB_3O_6$ at 298 and 81 K are listed in Table II and Table III, respectively. Table IV provides the structural parameters for the powder data at 100 K.

B. Charge density distributions

Figures 2(a) and 2(b) display the experimental charge density $\rho(\mathbf{r})$ obtained from SXRD at 298 and 81 K, respectively. Additionally, Figure 2(c) showcases the experimental $\rho(\mathbf{r})$ derived from the PXRD data. In all cases, the equidensity isosurfaces of the 3D $\rho(\mathbf{r})$ demonstrate satisfactory agreement with the corresponding atom arrangements. It is important to note that the experimental $\rho(\mathbf{r})$ represents a dynamic function that incorporates thermal effects. As depicted in Figure 2(a), the influence of thermal motion on the charge density is
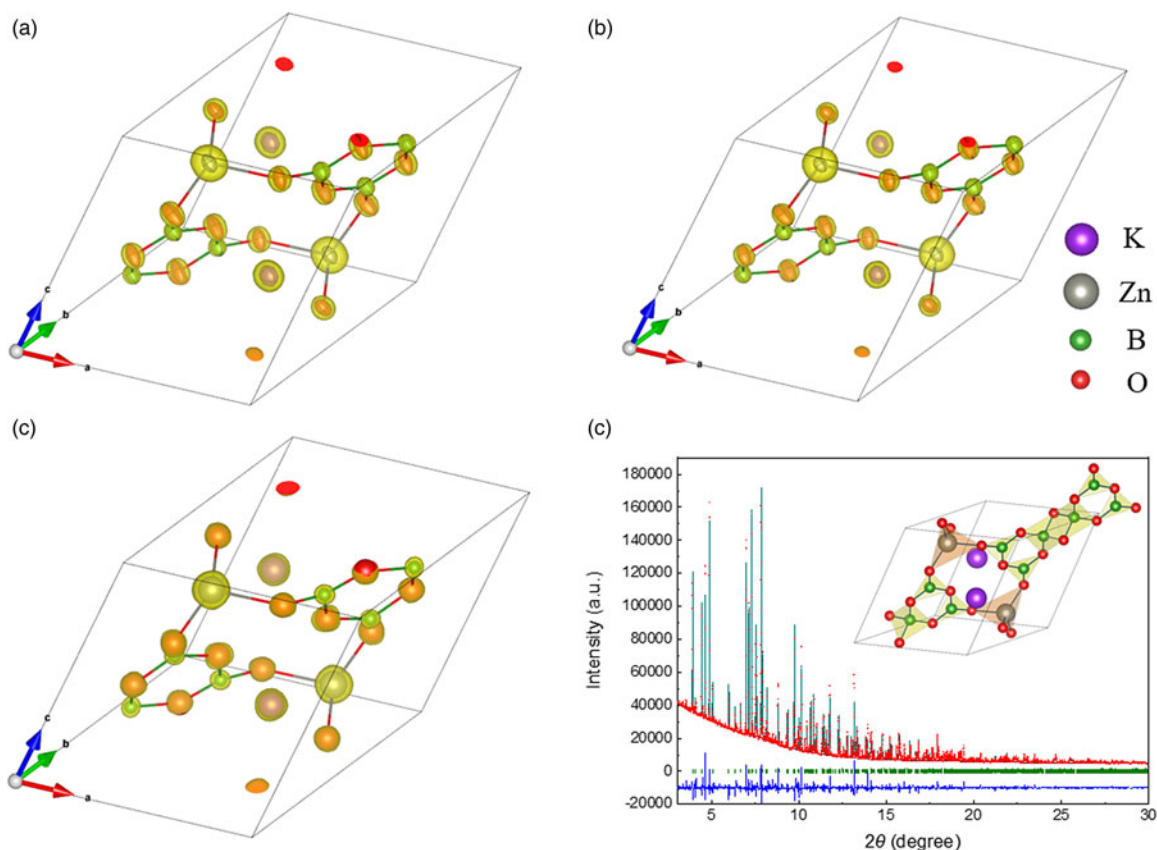

Figure 2. The single crystal structures of $KZnB_3O_6$ with anisotropic displacement parameters and corresponding three-dimensional EDD were obtained at 298 K (a) and 81 K (b). (c) The powder crystal structure of $KZnB_3O_6$ with isotropic displacement parameters collected at 100 K and the three-dimensional EDD. All the isosurface density levels of (a–c) are equal to 8 e/$Å^3$. (d) Comparison of the observed diffraction patterns (red point) of $KZnB_3O_6$ with the corresponding calculated patterns (green solid line). The lower green vertical bars show the Bragg positions. The difference curve is plotted in a blue solid line. Inset shows the structure of $KZnB_3O_6$, emphasizing the edge-sharing BO_4 units ($\lambda = 0.4255$ Å).

Experimental electron density distribution of $KZnB_3O_6$ constructed
by maximum-entropy method

TABLE I. Crystal data for KZnB$_3$O$_6$ refined by powder data at 100 K, single crystal data at 298 and 81 K, respectively

Chemical composition		KZnB$_3$O$_6$	
Space group		P-1	
Z		2	
Data set	Single crystal	Single crystal	Powder
Temperature (K)	298	81	100
a (Å)	6.753(6)	6.71885(7)	6.7575(1)
b (Å)	6.911(6)	6.93225(7)	6.9369(2)
c (Å)	7.045(7)	7.06511(7)	7.0833(1)
α (°)	63.39(5)	63.0978(10)	63.136(1)
β (°)	72.58(4)	71.9771(9)	72.407(1)
γ (°)	69.13(5)	68.9985(10)	69.072(1)
V (Å^3)	270.8(5)	269.646(6)	272.68(1)
D (Mg/m^3)	2.856	2.868	2.836

TABLE II. Structural parameters for single crystal KZnB$_3$O$_6$ at 298 K

Site	Wyckoff position	x	y	z	U_{iso} (Å^2)
Zn1	2i	0.67479(3)	0.85238(3)	0.12757(3)	0.01138(8)
K1	2i	0.25618(7)	0.79622(7)	0.57920(7)	0.01800(10)
O1	2i	0.8595(2)	0.5838(2)	0.0833(2)	0.0123(2)
O2	2i	0.7205(3)	0.8515(2)	0.3794(2)	0.0172(3)
O3	2i	0.6282(2)	1.1403(2)	−0.1186(2)	0.0133(2)
O4	2i	0.1980(2)	0.6715(2)	1.0324(2)	0.0157(3)
O5	2i	−0.1392(2)	0.6877(2)	0.7014(2)	0.0140(3)
O6	2i	0.6766(2)	1.4934(2)	−0.3663(2)	0.0160(3)
B1	2i	−0.2441(3)	0.6814(3)	0.5658(3)	0.0117(3)
B2	2i	0.7030(3)	1.3178(3)	−0.1674(3)	0.0115(3)
B3	2i	−0.0967(3)	0.5056(3)	0.9063(3)	0.0108(3)

TABLE III. Structural parameters for single crystal KZnB$_3$O$_6$ at 81 K

Site	Wyckoff position	x	y	z	U_{iso} (Å^2)
Zn1	2i	0.67478(2)	0.85345(2)	0.12717(2)	0.00343(1)
K1	2i	0.25708(2)	0.79482(2)	0.57922(2)	0.00572(2)
O1	2i	0.85841(6)	0.58281(6)	0.08507(6)	0.00460(5)
O2	2i	0.72082(7)	0.85370(6)	0.37875(6)	0.00626(5)
O3	2i	0.62986(6)	0.13955(6)	0.87876(6)	0.00499(5)
O4	2i	0.19877(6)	0.67137(6)	0.03234(6)	0.00574(5)
O5	2i	0.86029(6)	0.68892(6)	0.70182(6)	0.00521(5)
O6	2i	0.67698(6)	0.49446(6)	0.63201(6)	0.00579(5)
B1	2i	0.75585(9)	0.68266(8)	0.56535(8)	0.00459(6)
B2	2i	0.70310(8)	0.31776(8)	0.83151(8)	0.00454(6)
B3	2i	0.90284(8)	0.50654(8)	0.90595(8)	0.00451(6)

TABLE IV. Structural parameters for powder KZnB$_3$O$_6$ at 100 K

Site	Wyckoff position	x	y	z	U_{iso} (Å^2)
K1	2i	0.2579(4)	0.7977(4)	0.5763(4)	0.01267
Zn1	2i	0.6757(3)	0.8527(3)	0.1261(3)	0.01267
B1	2i	−0.236(2)	0.678(2)	0.549(2)	0.003(2)
B2	2i	0.690(2)	1.321(2)	−0.155(2)	0.003(2)
B3	2i	−0.096(2)	0.507(2)	0.916(2)	0.003(2)
O1	2i	0.862(1)	0.583(1)	0.082(1)	0.0099(9)
O2	2i	0.721(1)	0.851(1)	0.383(1)	0.0099(9)
O3	2i	0.626(1)	1.139(1)	−0.116(1)	0.0099(9)
O4	2i	0.200(1)	0.675(1)	1.024(1)	0.0099(9)
O5	2i	−0.140(1)	0.692(1)	0.697(1)	0.0099(9)
O6	2i	0.674(1)	1.491(1)	−0.367(1)	0.0099(9)

evident, with significant anisotropic thermal motion at 298 K causing expansion of the electron density isosurface along the stronger vibrational direction. Conversely, at 81 K, the electron density isosurface appears more isotropic due to reduced thermal effects, as shown in Figure 2(b). Meanwhile, in the PXRD case, while the crystal structures and $\rho(\mathbf{r})$ maps generally align, it is worth noting that the resulting thermal motion factors and $\rho(\mathbf{r})$ isosurfaces are larger than those obtained from the SXRD datasets. This observation suggests that the powder diffraction data provide the least precise $\rho(\mathbf{r})$ in the present study.

The most intriguing feature of KZnB$_3$O$_6$ lies in its edge-sharing B–O section, specifically the B$_6$O$_{12}$ block composed of two BO$_4$ tetrahedra and four BO$_3$ triangles. The BO$_4$

tetrahedra share edges with each other and are further connected to BO$_3$ triangles at their outer vertices (see the insert in Figure 2(d)). In Figure 3, we present two-dimensional slices of the charge density distribution in the B$_3$O$_3$ ring and B$_2$O$_2$ ring, obtained from the synchrotron PXRD data at 100 K, as well as the SXRD data at 298 and 81 K.

From Figures 3(a)–3(c), all illustrate the experimental $\rho(\mathbf{r})$ of the corner-shared B–O hexatomic ring, which is a common structural motif in borate crystals. The center of the six atoms is clearly visible in the $\rho(\mathbf{r})$ map, which is projected onto the (−1.43433, 1, 1.03254) plane intersecting the B$_3$O$_3$ ring. To enhance the visualization of charge density in the bonding region, the $\rho(\mathbf{r})$ range is limited to values lower than 1.5 e/Å^3. Additionally, we observe an obvious electron segregation
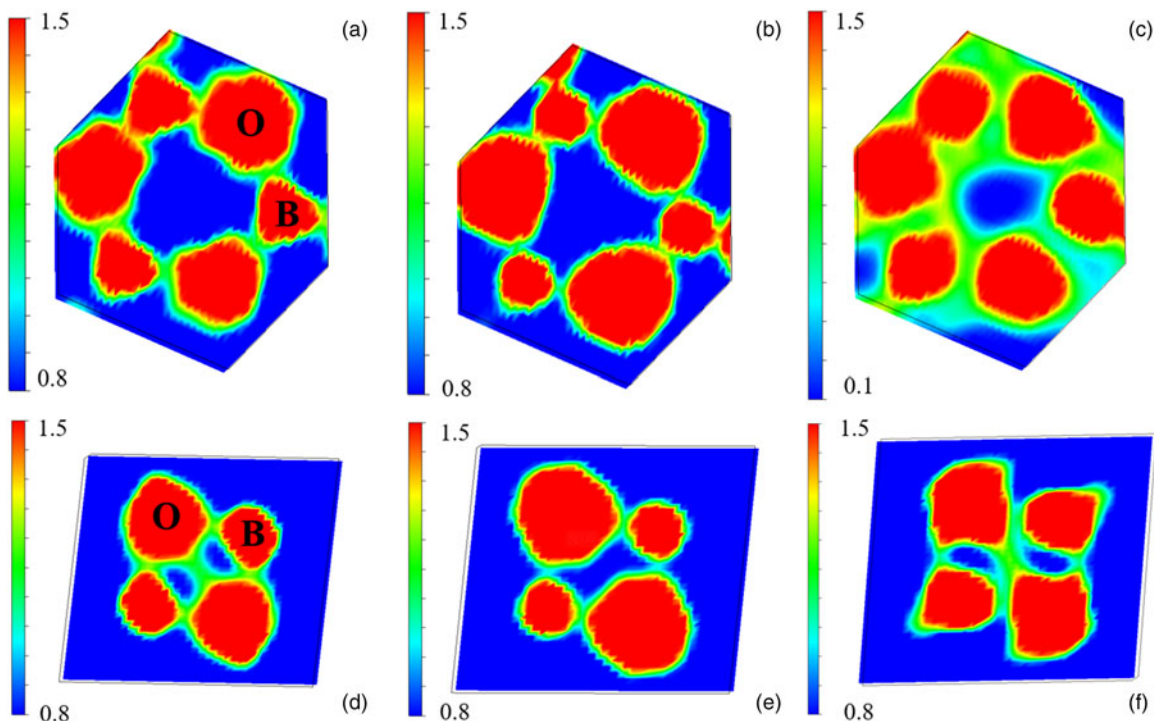
Figure 3. Two-dimensional slices of experimental $\rho(\mathbf{r})$ in the B_3O_3 ring were obtained from (a) single crystal data at 298 K, (b) single crystal data at 81 K, and (c) powder data at 100 K. Two-dimensional slices of experimental $\rho(\mathbf{r})$ in the B_2O_2 ring were obtained from (d) single crystal data at 298 K, (e) single crystal data at 81 K, and (f) powder data at 100 K. Each subgraph is plotted using the same charge density ranges.

within the B_3O_3 ring in the bonding region, indicative of the involvement of p atomic orbitals in the formation of covalent bonds. Notably, in the bonding region of the B–O hexatomic ring, the charge density obtained from the PXRD data becomes discontinuous at the lower level of 0.8 e/Å^3, confirming it is not as precise as the results from the SXRD data.

To investigate the nature of bond interactions in the edge-sharing region, we present the $\rho(\mathbf{r})$ map in the (1.13693, 2.90022, −1) plane intersecting the B_2O_2 ring (from Figures 3(d)–3(f)). In this plane, the two heavier atoms with higher

$\rho(\mathbf{r})$ values correspond to the O element, while the smaller two atoms represent B. Similar to the observations in the B–O hexatomic ring, we observe distinct electron segregation within the B_2O_2 ring in the B–O bonding region, indicating the involvement of p atomic orbitals in the formation of covalent bonds. Interestingly, both the room temperature SXRD data and the cryogenic synchrotron PXRD data reveal a fascinating phenomenon: the edge-shared B_2O_2 ring exhibits a significant accumulation of charge density between the O atoms. This unconventional O–O bonding is unexpected, as O–O
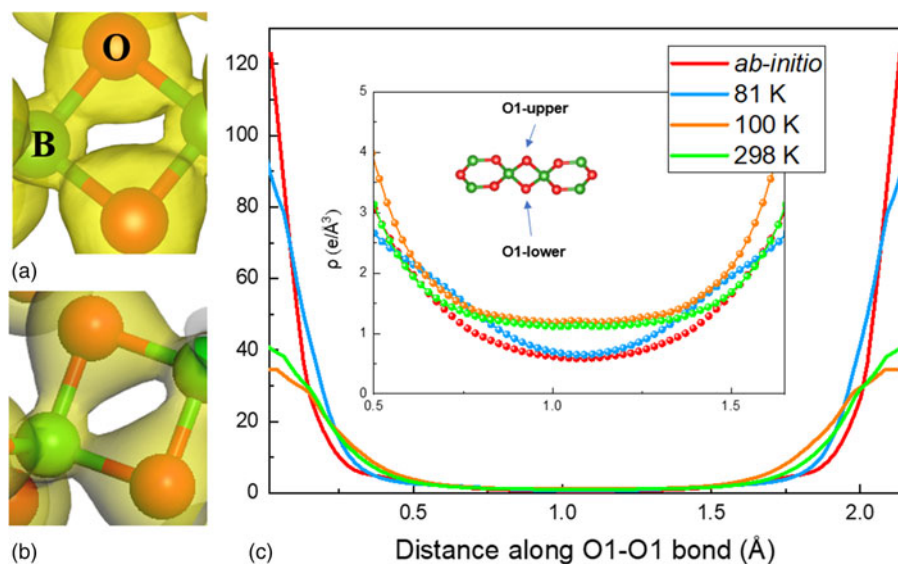

Figure 4. Three-dimensional charge density distribution of B_2O_2 ring obtained by single crystal diffraction at 81 K (a) and *ab-initio* calculations (b), with isosurface density level at 0.8 e/Å^3. (c) The one-dimensional electron density profiles along the O1–O1 bond in the B_2O_2 ring in various conditions. The inset shows the enlarged view of electron density.

Experimental electron density distribution of KZnB$_3$O$_6$ constructed by maximum-entropy method   237

covalent bonds are primarily observed in organic compounds. Such O–O covalence bonds are less common in inorganic systems, typically limited to certain metal peroxides and superoxides.

However, based on the high-quality SXRD data, it was demonstrated that the unusually accumulated electrons in the O–O bonding region are absent. The SXRD data at 81 K, with its high resolution ($d_{min} = 0.50$) and high signal-to-noise ratio ($I/\sigma(I) = 78$), provide more reliable charge density information. As shown in Figure 3(e), electron accumulation is observed solely in the B–O bond region within the edge-sharing B_2O_2 ring, suggesting that chemical bonding is still predominantly governed by B–O sp^3 bonding. This finding is consistent with the results of theoretical calculations performed using the experimental cell parameter of 81 K SXRD data, as illustrated in Figures 4(a) and 4(b). The one-dimensional electron density profiles along the O1–O1 bond in the B_2O_2 ring obtained by three experiments are compared with *ab-initio* calculations in Figure 4(c), demonstrating that electron density from the 81 K SXRD data is of the most accurate, while the PXRD provides the worst accuracy. Furthermore, to study the topology of charge density, the critical point in the middle of the B_2O_2 ring was calculated with the aid of the EDMA program (van Smaalen et al., 2003). A critical point of (3, +1) is found in both 81 and 298 K SXRD, which means the center of a ring structure without chemical bonding. However, the 100 K PXRD gives a critical point of (3, −1), showing the feature of a chemical bond. Considering all these factors above, the electron density obtained by the 81 K SXRD is the most plausible. Hence, it is evident that high-quality SXRD data collected at low temperatures is crucial in obtaining reliable experimental $\rho(\mathbf{r})$ values for $KZnB_3O_6$ using MEM.

IV. CONCLUSIONS

In conclusion, our study successfully constructed the experimental charge density of $KZnB_3O_6$ using the maximum-entropy method, incorporating both synchrotron powder diffraction and laboratory single crystal diffraction data. In the current case, the room temperature single crystal diffraction data and the cryogenic synchrotron powder diffraction data only lead to inaccurate charge density distributions. By utilizing cryogenic single crystal diffraction data with a higher signal-to-noise ratio and resolution limit, we obtained an accurate experimental EDD of $KZnB_3O_6$. The later EDD demonstrated excellent agreement with the results obtained from theoretical calculations. Our results highlight the significance of collecting high-quality diffraction data to obtain reliable experimental electron density information. The findings also contribute to a better understanding of the bonding interactions and electron distribution in borate crystals.

V. DEPOSITED DATA

The single crystal and powder data were deposited with ICDD. The data can be requested by contacting pdj@icdd.com. The single crystal data at 298 K, 81 K, and the powder data at 100 K are also deposited as Crystallographic Information Files.

REFERENCES

Delley, B. 2000. "From Molecules to Solids with the DMol³ Approach." *Journal of Chemical Physics* 113 (18): 7756–64. doi:10.1063/1.1316015.

Dolomanov, O. V., L. J. Bourhis, R. J. Gildea, J. A. K. Howard, and H. Puschmann. 2009. "*OLEX2*: A Complete Structure Solution, Refinement and Analysis Program." *Journal of Applied Crystallography* 42 (2): 339–41. doi:10.1107/S0021889808042726.

George, J., D. Waroquiers, D. Di Stefano, G. Petretto, G.-M. Rignanese, and G. Hautier. 2020. "The Limited Predictive Power of the Pauling Rules." *Angewandte Chemie* 132 (19): 7639–45. doi:10.1002/ange.202000829.

He, M., X. Chen, H. Okudera, and A. Simon. 2005. "$(K_{1-x}Na_x)_2Al_2B_2O_7$ with $0 \le X < 0.6$: A Promising Nonlinear Optical Crystal." *Chemistry of Materials* 17 (8): 2193–96.

Huppertz, H., and B. von der Eltz. 2002. "Multianvil High-Pressure Synthesis of $Dy_4B_6O_{15}$: The First Oxoborate with Edge-Sharing BO_4 Tetrahedra." *Journal of the American Chemical Society* 124 (32): 9376–77. doi:10.1021/ja017691z.

Izumi, F. 2004. "Beyond the Ability of Rietveld Analysis: MEM-Based Pattern Fitting." *Solid State Ionics*. Proceedings of the Fifteenth International Symposium on the Reactivity of Solids 172 (1): 1–6. doi:10.1016/j.ssi.2004.04.023.

Izumi, F., and K. Momma. 2007. "Three-Dimensional Visualization in Powder Diffraction." *Solid State Phenomena* 130 (December): 15–20. https://doi.org/10.4028/www.scientific.net/ssp.130.15.

Jain, A., S. P. Ong, G. Hautier, W. Chen, W. D. Richards, S. Dacek, S. Cholia, *et al.* 2013. "Commentary: The Materials Project: A Materials Genome Approach to Accelerating Materials Innovation." *APL Materials* 1 (1): 011002. doi:10.1063/1.4812323.

Jin, S., G. Cai, W. Wang, M. He, S. Wang, and X. Chen. 2010. "Stable Oxoborate with Edge-Sharing BO_4 Tetrahedra Synthesized under Ambient Pressure." *Angewandte Chemie International Edition* 49 (29): 4967–70. doi:10.1002/anie.200907075.

Lou, Y., D. Li, Z. Li, S. Jin, and X. Chen. 2015a. "Unidirectional Thermal Expansion in Edge-Sharing BO_4 Tetrahedra Contained $KZnB_3O_6$." *Scientific Reports* 5 (1): 10996.

Lou, Y., D. Li, Z. Li, H. Zhang, S. Jin, and X. Chen. 2015b. "Unidirectional Thermal Expansion in $KZnB_3O_6$: Role of Alkali Metals." *Dalton Transactions* 44 (46): 19763–67.

Momma, K., and F. Izumi. 2008. "*VESTA*: A Three-Dimensional Visualization System for Electronic and Structural Analysis." *Journal of Applied Crystallography* 41 (3): 653–58. doi:10.1107/S0021889808012016.

Momma, K., T. Ikeda, A. A. Belik, and F. Izumi. 2013. "Dysnomia, a Computer Program for Maximum-Entropy Method (MEM) Analysis and Its Performance in the MEM-Based Pattern Fitting." *Powder Diffraction* 28 (3): 184–93. doi:10.1017/S088571561300002X.

Mutailipu, M., K. R. Poeppelmeier, and S. Pan. 2020. "Borates: A Rich Source for Optical Materials." *Chemical Reviews* 121 (3): 1130–1202.

Netzel, J. 2008. *Accurate Charge Densities of Amino Acids and Peptides by the Maximum Entropy Method*. Bayreuth, Bavaria, Southeastern Germany: Universitaet Bayreuth (Germany).

Pauling, L. 1929. "The Principles Determining the Structure of Complex Ionic Crystals." *Journal of the American Chemical Society* 51 (1–4): 1010–26. doi:10.1021/ja01379a006.

Rietveld, H. M. 1967. "Line Profiles of Neutron Powder-Diffraction Peaks for Structure Refinement." *Acta Crystallographica* 22 (1): 151–52. doi:10.1107/S0365110X67000234.

Ross, V. F., & J. O. Edwards. 1967. "The Chemistry of Boron and Its Compounds." The Chemistry of Boron and Its Compounds, by Earl L. Muetterties, 155–207.

Sheldrick, G. M. 2008. "A Short History of *SHELX*." *Acta Crystallographica Section A Foundations of Crystallography* 64 (1): 112–22. doi:10.1107/S0108767307043930.

Smaalen, S. V., L. Palatinus, and M. Schneider. 2003. "The Maximum-Entropy Method in Superspace." *Acta Crystallographica Section A* 59 (5): 459–69. doi:10.1107/S010876730301434X.

Takata, M., E. Nishibori, and M. Sakata. 2001. "Charge Density Studies Utilizing Powder Diffraction and MEM. Exploring of High Tc Superconductors, C_{60} Superconductors and Manganites." *Zeitschrift Für Kristallographie – Crystalline Materials* 216 (2): 71–86. doi:10.1524/zkri.216.2.71.20335.

Wang, G., and X. Chen. 2010. "Single-Crystal Growth: From New Borates to Industrial Semiconductors." *Physica Status Solidi (a)* 207 (12): 2757–68.

Wu, L., X. L. Chen, Y. P. Xu, and Y. P. Sun. 2006. "Structure Determination and Relative Properties of Novel Noncentrosymmetric Borates $MM'_4(BO_3)_3$ (M=Na, M'=Ca and M=K, M'=Ca, Sr)." *Inorganic Chemistry* 45 (7): 3042–47.

Wu, Y., J.-Y. Yao, J.-X. Zhang, P.-Z. Fu, and Y.-C. Wu. 2010. "Potassium Zinc Borate, $KZnB_3O_6$." *Acta Crystallographica Section E* 66 (5): i45. doi:10.1107/S1600536810015175.

Xu, Z., X. Liu, D. Deng, Q. Wu, L.-a. Wu, B. Wu, S. Lin, B. Lin, C. Chen, and P. Wang. 1995. "Multiwavelength Optical Parametric Amplification with Angle-Tuned Lithium Triborate." *JOSA B* 12 (11): 2222–28.

Yang, L., W. Fan, Y. Li, H. Sun, L. Wei, X. Cheng, and X. Zhao. 2012. "Theoretical Insight into the Structural Stability of $KZnB_3O_6$ Polymorphs with Different BO_x Polyhedral Networks." *Inorganic Chemistry* 51 (12): 6762–70. doi:10.1021/ic300469s.